G. L. FALKENHAGEN
Associate Professor,
Department of Mechanical Engineering,
University of Idaho,
Moscow, Idaho

E. J. GUNTER
Associate Professor,
Department of Mechanical Engineering,
University of Virginia,
Charlottesville, Va.
Mem. ASME

F. T. SCHULLER
Bearing Branch,
NASA Lewis Research Center,
Cleveland, Ohio

Stability and Transient Motion of a Vertical Three-Lobe Bearing System

The stability characteristics and general transient motion of the finite-width three-lobe bearing assuming an incompressible fluid with cavitation are presented. The hydrodynamic bearing forces are evaluated by both a finite-difference analysis and an approximate method. The approximate method consists of the infinite bearing solution corrected for end leakage. The approximate method is compared to the finite-difference solution of Reynolds equation and yields acceptable accuracy while running 100 times faster. Linearized bearing stiffness and damping coefficients are determined numerically and used to calculate the threshold of instability for a rigid vertical rotor. The stability curves developed are compared to NASA experimental data as well as analytic work performed by Lund. The nonlinear transient orbits for a balanced rotor are computed and plotted for comparison to the linear stability curves and the NASA test data. The influence of rotor unbalance above and below the stability threshold is investigated. The stability of the three-lobe bearing is optimized with respect to minimum film thickness. It is found that the optimum preload factor varies from 0.59 to 0.47 and the corresponding offset factor ranges from 0.8 to 1.0 for an aspect ratio $L/D = 1.0$.

Introduction

The hydrodynamic multi-lobe bearing is used widely in high-speed rotating machinery because of its superior stability. To design a hydrodynamic bearing for a given application it is necessary to calculate a variety of bearing characteristics such as load carrying capacity, power loss, and in particular the stability of the rotor system. The steady-state load capacity and power losses of the multi-lobe bearing have been extensively investigated by Pinkus [1, 2].[1] In high-speed applications, the bearing load-carrying capacity is secondary in comparison to the rotor stability. Pinkus [3], in his experimental investigation of bearing stability, states that the order of bearing stability ranges from the three-lobe, tilting pad, elliptic, three groove down to the plain circular bearing. More recent studies show that in general the tilting pad bearing is the most stable configuration [4].

For vertical rotor systems or space power systems acting under zero-g conditions, the stability characteristics of the bearing are of paramount importance. For example the plain journal bearing is completely unstable in the vertical position for all speeds [5] while the multi-lobe bearing exhibits excellent stability characteristics [6, 7].

The stability criteria for a multi-lobe bearing was first developed by Lund [6] based on linearization of the Reynolds equation by small-perturbation theory. Lund provides considerable insight into the important design parameters governing stability and shows the effect of preload on stability.

In addition to the prediction of the stability threshold it is desirable to evaluate the complete rotor nonlinear transient motion for arbitrary loading. The development of a general transient analysis allows one to predict the maximum bearing forces transmitted and also the size of the journal limit cycle. The use of a time transient technique was first demonstrated by Castelli [8] in the analysis of the 360 deg plain gas journal bearing and has been extended into more complex models such as a tilting pad rotor system with 18 deg of freedom [9]. In both of these papers the hydrodynamic bearing forces are evaluated by a numerical solution of the Reynolds equation. Although this procedure is very accurate, it is extremely time-consuming and uneconomical to use as a basic design tool.

In this analysis, a time transient procedure is presented based on an approximate solution of the Reynolds equation which runs about 100 times faster than the numerical solution. It is thus possible with this procedure to rapidly and economically evaluate various rotor-bearing design configurations.

Bearing Film Thickness

The geometry of a partial journal bearing is shown in Fig. 1 and the film thickness expression in polar coordinates is given by

[1] Numbers in brackets designate References at end of paper.

Contributed by the Lubrication Division and presented at the Vibrations Conference, Toronto, Canada, September 8–10, 1971, of The American Society of Mechanical Engineers. Manuscript received at ASME Headquarters, June 4, 1971. Paper No. 71-Vibr-76.

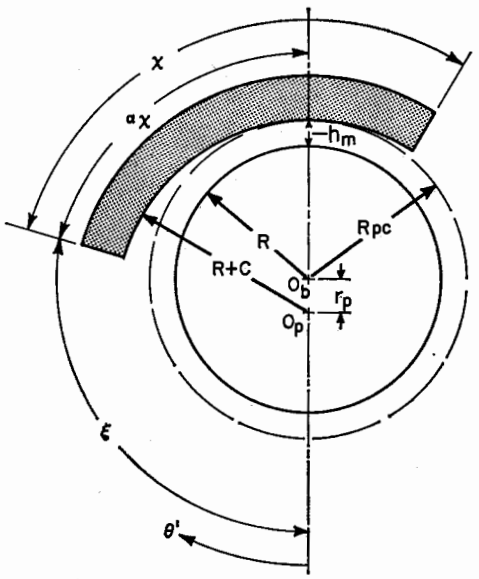

Fig. 1 Individual shoe–shaft bearing geometry

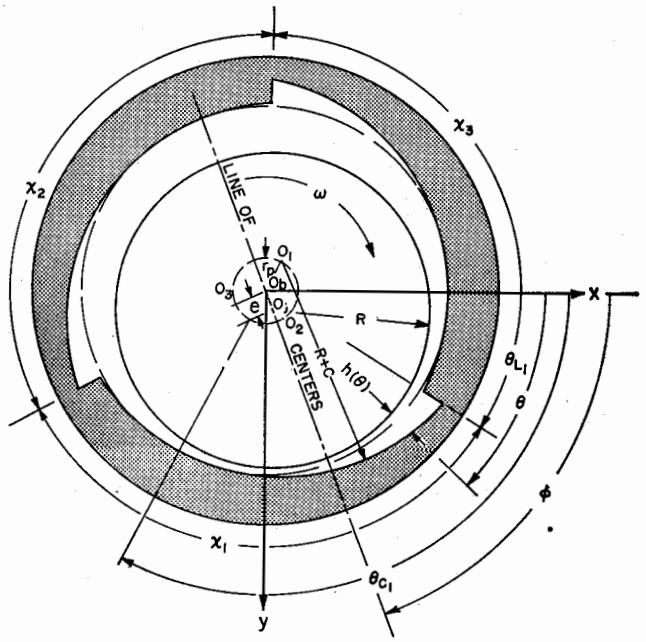

Fig. 2 Multi-lobe journal bearing

$$h(\theta') = C[1 + \epsilon \cos \theta']; \quad \xi \leq \theta' \leq \xi + \chi \qquad (1)$$

The multi-lobe bearing may be considered as n partial journal bearings oriented about the shaft in a fixed configuration. The multi-lobe bearing of Fig. 2 is composed of three partial arcs that are preloaded a distance r_p along a radial line located at θ_c.

The film thickness representation in polar coordinates would appear to be a logical choice for the multi-lobe bearing since analytical solutions of the individual bearing sector steady-state load capacities are most readily obtained with this coordinate system. However, in the case of dynamic studies of rotor-bearing motion, the bearing line of centers is not stationary, but precesses. This leads to a set of rotating coordinates for the film thickness representation which is difficult to generalize for higher-order bearing systems such as a multi-lobe or a spring-loaded tilting pad bearing.

Castelli has demonstrated in his analysis of the plain gas journal bearing [8] and tilting pad bearing rotor system [9] that it is convenient to represent the dynamical equations of motion and the film thickness expressions in terms of fixed cartesian coordinate formulation. Also, Kirk and Gunter [5], using the cartesian formulation, have recently analyzed the transient dynamics of the plain journal bearing.

The film thickness for the multi-lobe bearing is derived in Appendix A and is given as follows:

$$h(\theta) = C - X \cos \theta - Y \sin \theta - r_p \cos (\theta_c - \theta) \qquad (2)$$

The dimensionless film thickness may be expressed in terms of the preload factor $\delta = r_p/c$ and the sector offset factor as follows:

$$H(\theta) = 1 - X \cos \theta - Y \sin \theta - \delta \cos (\theta_{Li} + \alpha\chi - \theta); \quad \theta_{Li} \leq \theta \leq \theta_{Li} + \chi \qquad (3)$$

Solution of Reynolds Equation

Numerical Solution. The equation governing the hydrodynamic pressure developed in a multi-lobe bearing for an incompressible lubricant is given by the well-known Reynolds equation in fixed coordinates as follows [7]:

$$\frac{\partial}{\partial \theta}\left[H^3 \frac{\partial p}{\partial \theta}\right] + \left(\frac{R}{L}\right)^2 \frac{\partial}{\partial \eta}\left[H^3 \frac{\partial p}{\partial \eta}\right] = \lambda\left[\frac{\partial H}{\partial \theta} + 2\frac{\partial H}{\partial T}\right] \qquad (4)$$

where

$$\lambda = 6\mu\omega\left(\frac{R}{C}\right)^2$$

Nomenclature

R = bearing radius, in.
R_p = pad or sector radius
r_p = pad preload, in.
t = time, sec
T = ωt, dimensionless time
X, Y = displacement, in.
$\dot{X}, \dot{Y}$ = velocity in X and Y directions, in/sec
$\ddot{X}, \ddot{Y}$ = acceleration in X and Y directions, in/sec^2
$\alpha = \dfrac{\theta_c - \theta_L}{\chi}$, offset factor
$\beta = \xi + \chi$, angle between line of centers and lobe trailing edge
$\delta = r_p/c$, preload
$\epsilon = e/c$, eccentricity ratio
$\eta = Z/L$
θ = angular displacement measured from X axis in direction of journal rotation, rad
θ' = angular displacement measured from line of centers in direction of journal rotation, rad
θ_c = angle from X axis to individual lobe line of centers, rad
θ_L = angle from X axis to pad leading edge, rad
θ_X = angular displacement of the shaft projected into the X-Z plane, rad
θ_Y = angular displacement of the shaft projected into the Y-Z plane, rad
$\lambda = 6\mu\omega\left(\dfrac{R}{C}\right)^2$, psi
ν = whirl frequency, rad/sec
ξ = angle from line of centers to lobe leading edge, rad
χ = lobe arc length, rad
$\psi = pH$, psi
ω = angular velocity, rad/sec
$\Omega = 6\mu\omega L\left(\dfrac{R}{C}\right)^2$

The numerical solution of the Reynolds equation has been extensively reported by various investigators such as Raimondi and Boyd [10], Pinkus [11], and Castelli [12]. The numerical method chosen in this work is similar to a numerical method described by Castelli and Pirvics [13]. The pressure solution is obtained by performing N inversions of an $M \times N$ matrix, where M is the number of axial grid divisions and N is the number of circumferential divisions, and as Castelli points out, the running time is proportional to $N \times M^3$. To attain acceptable accuracy while keeping running time to a minimum, a grid size of 24×6 was chosen for each sector of the three-lobed bearing.

Letting $\psi = pH$, the Reynolds equation in del notation may be expressed as follows:

$$\nabla^2\psi + \frac{\nabla\psi \cdot \nabla H}{H} - \frac{\psi}{H^2}\left[(\nabla H)^2 + H\nabla^2 H\right] - \frac{\lambda}{H^2}\left[\frac{\partial H}{\partial \theta} + 2\frac{\partial H}{\partial T}\right] = 0 \quad (5)$$

Using the following time-discretized model

$$\nabla^2\psi^{(n+1)} = G(\psi, H)^{(n)}$$

where (n) refers to time T and $(n+1)$ refers to time $T + \Delta T$.

Using the standard three-point finite-difference equations, and upon rearranging, the finite-difference form of the incompressible Reynolds equation becomes:

$$\psi(i+1, j) - 2\left[1 + \left(\frac{R}{L}\right)^2\left(\frac{\Delta\theta}{\Delta Z}\right)^2\right]\psi(i, j) + \psi(i-1, j) + \left(\frac{R}{L}\right)^2\left(\frac{\Delta\theta}{\Delta Z}\right)^2\psi(i, j+1) + \left(\frac{R}{L}\right)^2\left(\frac{\Delta\theta}{\Delta Z}\right)^2\psi(i, j-1) = (\Delta\theta)^2 G(i, j) \quad (6)$$

The above finite-difference equation may be solved by the implicit columnwise influence coefficient method of [13]. The appropriate boundary conditions for equation (6) for the $N \times M$ grid are:

$$\psi(i, 1) = \psi(i, M) = \psi(1, j) = \psi(N, j) = 0 \quad (7)$$

since the pressure at the boundaries of each sector of the multilobed bearing is ambient and p is measured relative to the ambient pressure.

The numerical solution to equation (6) is used as a comparison to the results obtained by the approximate method developed in the following section.

Approximate Solution. The numerical solution of the Reynolds equation for the finite-width bearing is very accurate but is too time-consuming to use for general time transient studies of rotor-bearing systems. Thus, the development of a rapid means of approximating the hydrodynamic bearing forces is essential in order to feasibly evaluate the nonlinear shaft orbital motion with arbitrary loading. An approximate solution to equation (4) can be obtained by determining the pressure profile for the infinite bearing, and then modifying the infinite bearing solution with an end-leakage correction factor in a manner similar to that described by Pitts [14], and developed in Appendix B

$$p(\theta, Z) = p_\infty\left[1 - \frac{\cosh\frac{KL\eta}{R}}{\cosh\frac{KL}{D}}\right] \quad (8)$$

where p_∞ is determined from the solution of the reduced Reynolds equation for the infinitely wide bearing given by:

$$\frac{\partial}{\partial\theta}\left[H^3\frac{\partial p}{\partial\theta}\right] = \lambda\left[\frac{\partial H}{\partial\theta} + 2\frac{\partial H}{\partial T}\right] \quad (9)$$

The infinite bearing solution for general shaft motion is:

$$p_\infty(\theta) = \lambda\left[\int_{\theta_1}^{\theta}\frac{d\theta}{H(\theta)^2} + 2\int_{\theta_1}^{\theta}\frac{(-\dot{X}\sin\theta + \dot{Y}\cos\theta)}{H^3}\,d\theta - \frac{I_1}{I_2}\int_{\theta_1}^{\theta}\frac{d\theta}{H^3}\right] \quad (10)$$

where

$$I_1 = \int_{\theta_1}^{\theta_2}\frac{d\theta}{H^2} + \int_{\theta_1}^{\theta_2}\frac{(-\dot{X}\sin\theta - \dot{Y}\cos\theta)}{H^3}\,d\theta \quad (11)$$

$$I_2 = \int_{\theta_1}^{\theta_2}\frac{d\theta}{H^3} \quad (12)$$

The integrals I_1 and I_2 are evaluated for each bearing segment from the arc leading edge to the sector trailing edge. The integrals I_1 and I_2 and equation (10) for the infinite bearing pressure p_∞ are solved numerically with the digital computer. Since equation (10) is evaluated numerically, cavitation is considered by excluding all negative pressures.

Hydrodynamic Forces

The hydrodynamic force components exerted by the bearing on the shaft in fixed cartesian coordinates are obtained as follows:

$$\begin{Bmatrix} F_X \\ F_Y \end{Bmatrix} = -\sum_{i=1}^{N}\int_{-\frac{L}{2}}^{\frac{L}{2}}\int_{\theta_{Li}}^{\theta_{Li}+\psi_i} p(\theta, Z)R\begin{Bmatrix}\cos\theta \\ \sin\theta\end{Bmatrix}d\theta\,dZ \quad (13)$$

The pressure distribution, for the case of the approximate solution, can be integrated across the bearing width. The bearing forces thus will be a function only of the infinite fluid film pressure profile integrated over the bearing sectors multiplied by an end leakage factor I_Z as follows:

$$\begin{Bmatrix} F_X \\ F_Y \end{Bmatrix} = -RL\sum_{i=1}^{n} I_{Zi}\int_{\theta_{Li}}^{\theta_{Ti}} p_\infty(\theta)\begin{Bmatrix}\cos\theta \\ \sin\theta\end{Bmatrix}d\theta \quad (14)$$

where

$$I_{Zi} = \left[1 - \frac{D}{K_i L}\tanh\frac{K_i L}{D}\right] \quad (15)$$

The end-leakage correction factor K_i for the ith sector is developed in Appendix B and is given as follows:

$$K_i = \sqrt{\left(\frac{\pi}{\chi}\right)^2 + \left(\frac{A}{2}\right)^2 + B} \quad (16)$$

where

$$A = \frac{1}{\chi}\int_{\xi_i}^{\beta_i}\frac{\epsilon_i\sin\theta'}{1 + \epsilon_i\cos\theta'}\,d\theta' \quad (17)$$

$$B = \frac{1}{\chi}\int_{\xi_i}^{\beta_i}\left[A^2 - \frac{\epsilon_i\cos\theta'}{1 + \epsilon_i\cos\theta'}\right]d\theta' \quad (18)$$

The total force is given by:

$$F_T = \sqrt{F_X^2 + F_Y^2} \quad (19)$$

Fig. 3 represents the relationship between the end-leakage factor I_Z and the parameter K for various values of bearing aspect ratios. For aspect ratios of $L/D > 2.0$, and for large eccentricities, the end-leakage factor approaches unity which represents the infinite bearing solution. Notice that for the case of the narrow aspect ratio of 0.25, the bearing load capacity is no more than 5 to 10 percent of the finite bearing solution.

To further evaluate the accuracy of the approximate method

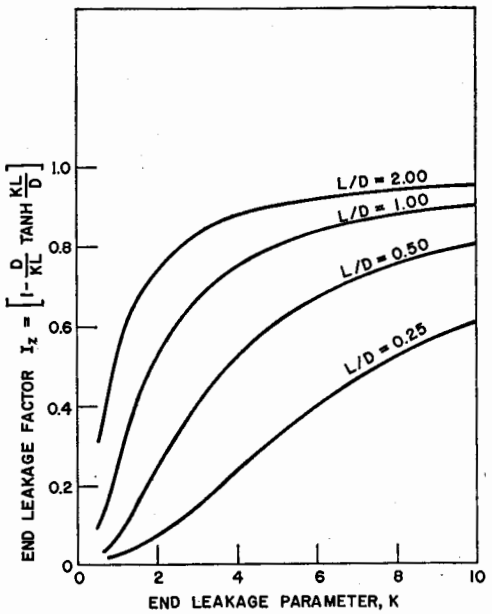

Fig. 3 Integrated end-leakage factor versus end-leakage parameter for various bearing aspect ratios

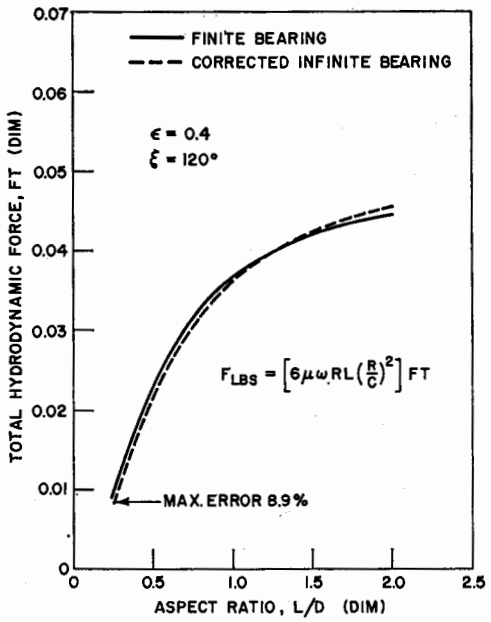

Fig. 4 Total hydrodynamic forces for finite bearing and infinite bearing corrected for end leakage for a 120 deg partial arc bearing

for the prediction of the hydrodynamic bearing forces, the load capacity and attitude angle for various eccentricity and aspect ratios were compared to the values obtained from the numerical solution [7]. For example, Fig. 4 compares the total hydrodynamic forces acting on a 120 deg partial bearing obtained from the numerical finite bearing solution and the corrected infinite bearing solution for various aspect ratios. For this particular case of $\epsilon = 0.4$ the largest deviation in the approximate solution occurs at small aspect ratios and does not exceed 10 percent. At higher eccentricities the load capacity predicted by the approximate solution is conservative and is 10 to 20 percent below previously published values [16].

Stability of a Vertical Rotor

The general equations of motion for the unbalanced rotor of Fig. 5 are:

$$-M\ddot{X} + F_X(X, Y, \dot{X}, \dot{Y}) = -M(e_M\omega^2 \cos \omega t - e_M\phi \sin \ddot{\phi}) \quad (20)$$

$$-M\ddot{Y} + F_Y(X, Y, \dot{X}, \dot{Y}) = -M(e_M\omega^2 \sin \omega t + e_M\ddot{\phi} \cos \phi) \quad (21)$$

For a balanced rotor with negligible rotor acceleration the right-hand side of equations (20) and (21) vanishes and the equations of motion become:

$$-M\ddot{X} + F_X(X, Y, \dot{X}, \dot{Y}) = 0 \quad (22)$$

$$-M\ddot{Y} + F_Y(X, Y, \dot{X}, \dot{Y}) = 0 \quad (23)$$

For small displacements and velocities about the origin equations (22) and (23) can be approximated by [17]:

$$M\ddot{X} + C_{XX}\dot{X} + C_{XY}\dot{Y} + K_{XX}X + K_{XY}Y = 0 \quad (24)$$

$$M\ddot{Y} + C_{YX}\dot{X} + C_{YY}\dot{Y} + K_{YX}X + K_{YY}Y = 0 \quad (25)$$

The total stiffness and damping coefficients for a multi-lobe bearing may be computed numerically by evaluating the changes in hydrodynamic forces caused by small velocity and displacement perturbations about the bearing center. The stiffness and displacement perturbations about the bearing center, The stiffness and damping coefficients are given by:

$$K_{ij} = -\frac{1}{2\Delta j}[F_i(\Delta j) + F_i(-\Delta j)]; \quad i = X,Y; \quad j = X, Y \quad (26)$$

$$C_{ij} = -\frac{1}{2\Delta j}[F_i(\Delta j) + F_i(-\Delta j)]; \quad i = \dot{X}, \dot{Y}; \quad j = \dot{X}, \dot{Y} \quad (27)$$

The bearing stiffness and damping coefficients may be calculated using either the numerical finite-width bearing program or the computer program based on the approximate method.

The eight bearing coefficients obtained from equations (26) and (27) are compared to data computed by Lund [6] for a three-lobed bearing in Table 1. Lund computes the bearing coefficients by perturbation of the Reynolds equation in rotating coordinates. The minor discrepancies in the values of bearing coefficients are insignificant from an engineering standpoint.

At the threshold of instability X and Y are pure harmonic motions with a frequency of ν. Thus equations (24) and (25) can be written as:

$$\begin{bmatrix} (K_{XY} - M\nu^2 + i\nu C_{XY}) & (K_{XY} + i\nu C_{XY}) \\ (K_{YX} + i\nu C_{YX}) & (K_{YY} - M\nu^2 + i C_{YY}) \end{bmatrix} \begin{bmatrix} X \\ Y \end{bmatrix} = 0 \quad (28)$$

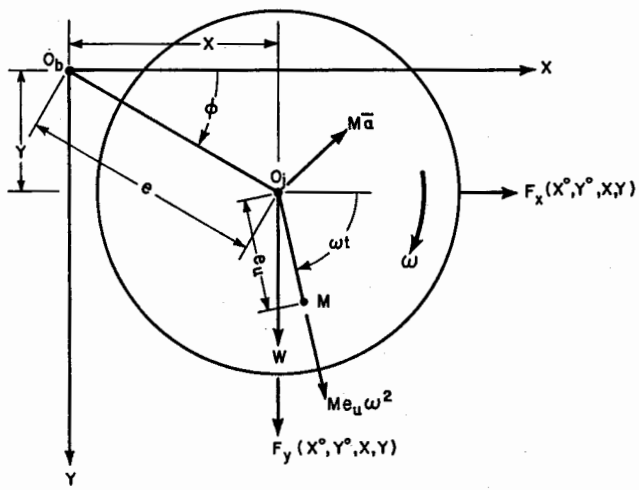

Fig. 5 Free-body diagram of a rigid unbalanced rotor

Table 1 Comparison of stiffness and damping coefficients to data of Lund for a three-lobed bearing supporting a vertical rotor, $\delta = 0.5$, Re = 0, $L/D = 1/2$

	Dimensionless Stiffness			
	$\overline{K_{XX}}$	$\overline{K_{YY}}$	$\overline{K_{XY}}$	$\overline{K_{YX}}$
Approx. method	0.24568	0.24690	0.40577	−0.40521
Lund [6]	0.25952	0.25952	0.36507	−0.36507

	Dimensionless Damping			
	$\overline{C_{XX}}$	$\overline{C_{YY}}$	$\overline{C_{XY}}$	$\overline{C_{YX}}$
Approx. method	0.77744	0.77787	0.00228	0.00085
Lund [6]	0.75925	0.75925	−0.00159	0.00159

These two equations have a nontrivial solution only when the determinant is zero. Equating the real and imaginary parts of the determinant to zero and using dimensionless stiffness and damping coefficients:

$$M\nu^2 = 6\mu\omega L\left(\frac{R}{C}\right)^3 \times\left[\frac{\bar{K}_{XX}\bar{C}_{YY} + \bar{K}_{YY}\bar{C}_{XX} - \bar{K}_{XY}\bar{C}_{YX} - \bar{K}_{YX}\bar{C}_{XY}}{\bar{C}_{XX} + \bar{C}_{YY}}\right] = \Omega\bar{D} \tag{29}$$

$$\nu^2 = \omega^2\left[\frac{(\bar{K}_{XX} - \bar{M}\nu^2)(\bar{K}_{YY} - \bar{M}\nu^2) + \bar{K}_{XY}\bar{K}_{YX}}{\bar{C}_{XX}\bar{C}_{YY} - \bar{C}_{XY}\bar{C}_{YX}}\right] = \omega^2\bar{\nu} \tag{30}$$

Equation 29 is first calculated and then substituted into equation (30) and ν^2 is also calculated. Upon dividing equation (29) by equation (30):

$$M = \frac{\Omega\bar{p}}{\omega^2\bar{\nu}} = \frac{6\mu L(R/\bar{C})^3}{\omega}\left(\frac{\bar{D}}{\bar{\nu}}\right) \tag{31}$$

Let the critical mass $\bar{M}$ be defined

$$\bar{M} = \frac{3}{2\pi}\left(\frac{\bar{D}}{\bar{\nu}}\right)$$

Solving equation (31) for the critical mass and converting the rotor speed to rps results in:

$$\bar{M} = \frac{MCN_{\text{rps}}}{\mu DL\left(\frac{R}{C}\right)^2} \tag{32}$$

The critical mass is a very useful design parameter since it gives a quantitative indication of threshold speed and shows the effect of rotor-bearing geometry on stability. The threshold speed is determined by solving equation (32) for N:

$$N_{\text{rpm}} = 120\,\mu L\left(\frac{\bar{M}}{M}\right)\left(\frac{R}{C}\right)^3 \tag{33}$$

Comparison of Theoretical and Experimental Values of Bearing Stability

Experimental data for a vertical rotor in a three-lobed bearing were obtained at the NASA Lewis Research Center for comparison to theoretical data [18]. The test facility depicted in Fig. 6 consists of a vertical rotor that has its weight supported by hydrostatic gas bearings. Motion perpendicular to the rotor centerline is constrained by the three-lobed self-acting bearing shown in Fig. 7. The bearing has a nominal diameter of 1.5 in. and is 1.5 in. long. In the experimental investigation, two types of bearings were tested, one with a converging–diverging film ($\alpha = 0.6$) and the second with a completely converging film geometry ($\alpha = 1.0$). The experimental program has shown that the completely converging film geometry is significantly more stable then the converging–diverging configuration.

The stability data from the testing of the converging–diverging film geometry using water at 80 deg F as a lubricant is tabulated in Table 2.

Fig. 8 represents the critical mass for a three-lobe vertical bearing versus preload for a converging–diverging fluid film geometry with sector arc lengths $\chi = 110$ deg and an aspect ratio $L/D = 1.0$. The experimental data are shown as circles plotted on Fig. 8. The theoretical values of stability or critical mass were calculated by three different methods. The first

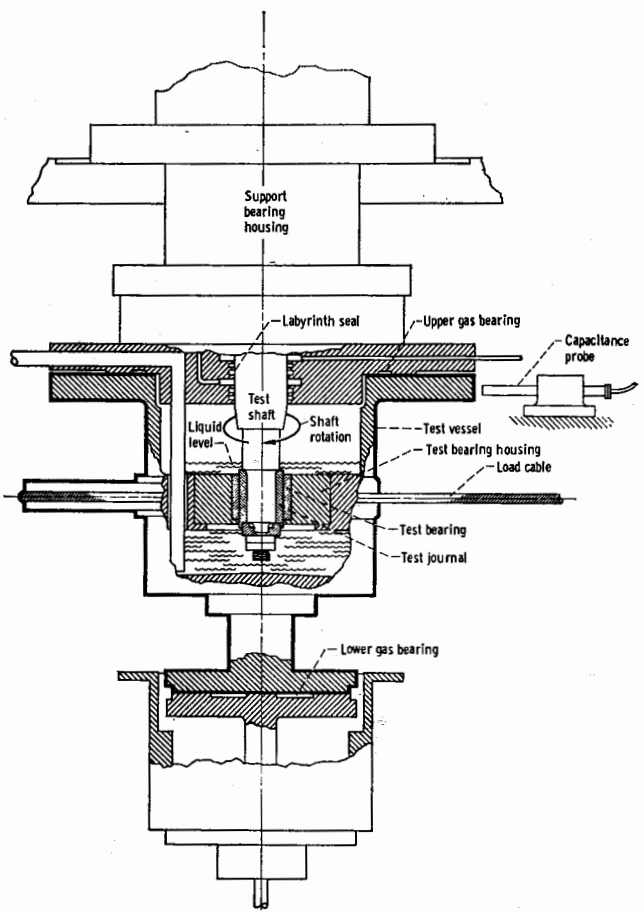

Fig. 6 Bearing test apparatus

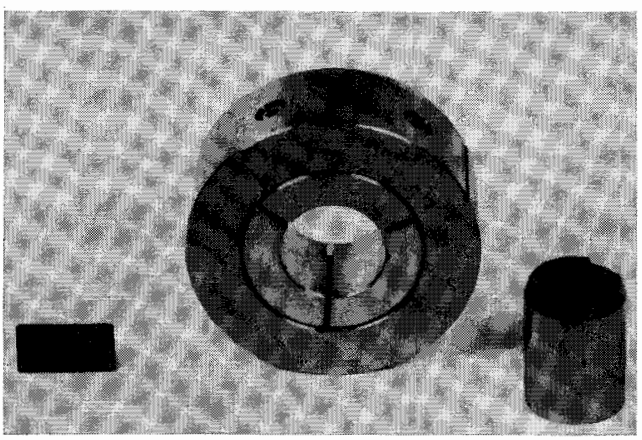

Fig. 7 Three-lobed bearing configuration

Table 2 Experimental data, $\alpha = 0.6$, $\chi = 110$ deg, $L/D = 1.0$, $M = 0.286$ lb-sec^2/in., $\mu = 13 \times 10^{-8}$ lb-sec/in.^{2}, $L = 1.5$ in., $D = 1.5$ in.

Preload factor $\delta = r_{p/c}$	Radius of clearance circle C (mil)	Threshold speed N_{rpm}	Critical mass, $\bar{M}$
0.32	3.1	290	.25
0.38	2.6	510	.26
0.48	2.1	2400	.64
0.57	5.1	460	1.71
0.66	4.4	600	1.48
0.70	6.6	800	7.63
0.74	3.9	1800	3.09
0.75	6.1	1200	7.84
0.78	10.0	300	8.65
0.82	5.6	2200	11.10
0.82	9.5	500	12.35
0.87	9.0	1200	25.20

procedure, denoted by the solid lines shown in Fig. 8, represents the stability threshold using the finite-width numerical computer program assuming large and small displacements. Note that with a large velocity perturbation the stability threshold is lower than that obtained with small displacements. The dotted line which falls between the upper and lower bound was obtained with the infinite-width multi-lobe bearing program corrected for end leakage and using small velocity perturbations.

As a further comparison, the stability threshold, as predicted by Lund, is shown as the dash–dot line and falls close to the approximate solution. The dashed curve was obtained by Lund for the same bearing configuration except the offset factor was 0.5 instead of 0.6 and the sector arc length was 100 deg. For the case of the larger offset value of $\alpha = 0.6$ and arc length of 110 deg, the Lund method would be expected to produce higher stability values. The procedure used by Lund to obtain the stability threshold was to perturb the Reynolds equation and solve for the linearized bearing forces.

Of particular interest is the observation that multiple stability thresholds can exist dependent upon the size of the velocity perturbation. The physical significance of this is that if the rotor is given a large impulse as it approaches the lower stability boundary it will exhibit a fractional frequency whirl orbit which will damp out. Therefore, between the upper and lower stability thresholds there seems to be a transition region where instability occurs as a function of the velocity terms. If the rotor is extremely well balanced and is given no external impulse then the rotor will not exhibit instability until it reaches the upper boundary as indicated by the line for small velocity perturbations. Above this line the rotor should become completely unstable. Upon reduction in speed it is possible that the rotor will not stabilize at the upper stability boundary but will stabilize at a lower speed depending on the size of the rotor orbit. Thus it is possible that there can be a hysteresis region in the observation of the stability boundary. This phenomenon has been observed with many experimental bearing configurations.

The trend of the experimental data is the same as for the various analytical methods. Some deviation of the experimental data from the analytic work may be due to the difficulty of accurately determining the bearing offset factor, preload, and clearances. For example, an error of 10 percent in measuring the bearing clearance would result in an error of over 30 percent in value of the critical mass. The experimental data generated for the wholly converging film show higher stability trends but with considerably more deviation from the analytical predictions.

Transient Orbits

The stability of a rotor-bearing system can be estimated by the previously mentioned linear analysis, but often it is desirable to calculate the complete transient path and the nonlinear limit

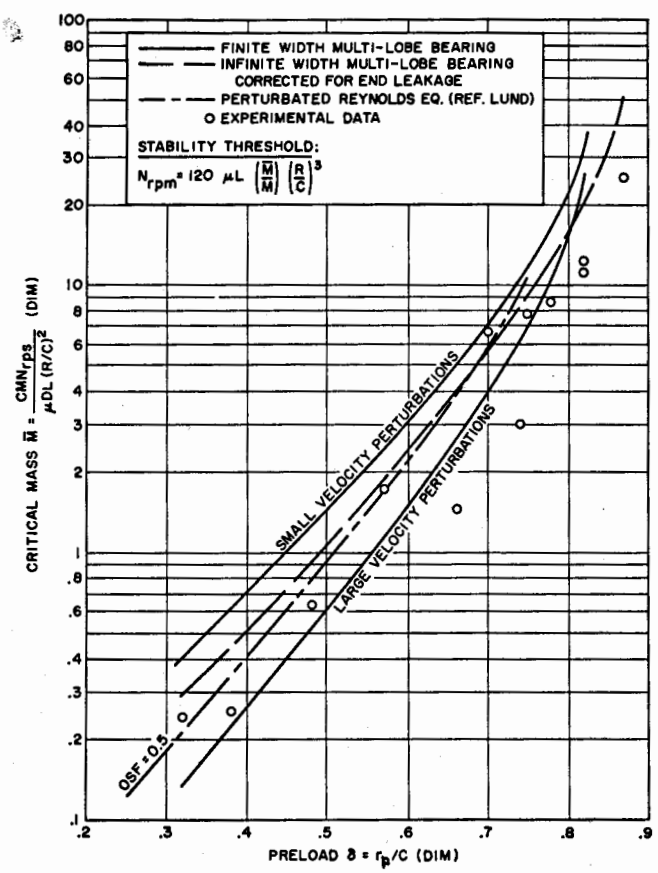

Fig. 8 Stability of a three-lobe vertical bearing versus preload for $L/D = 1.0$

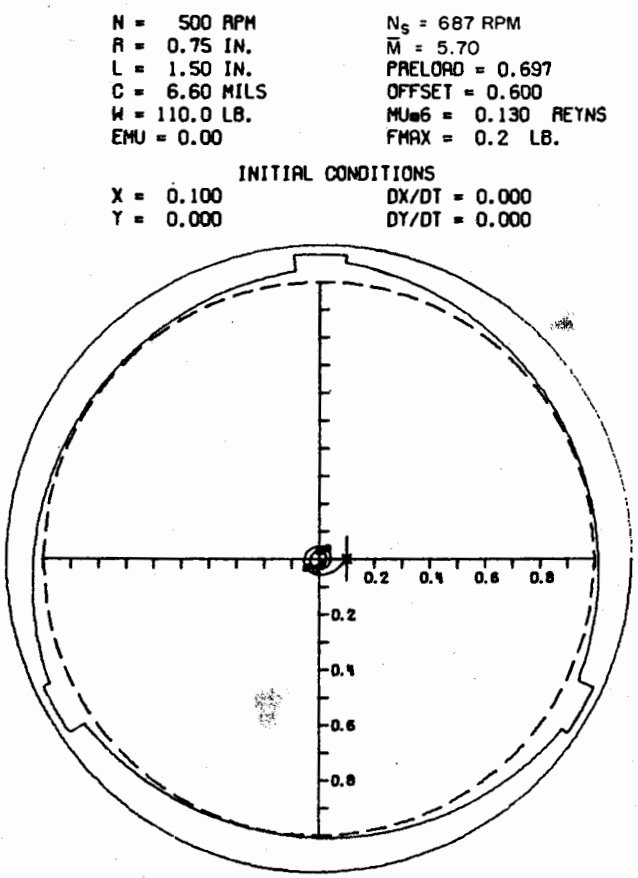

Fig. 9 Transient orbit of a balanced vertical rotor below the stability threshold, $N = 500$, $N_s = 687$ rpm

cycle of the rotor. The calculation of the rotor path provides additional information such as the magnitude and location of the maximum force transmitted to the bearing and the size of the rotor orbit. This form of analysis completely determines the system characteristics since it includes the steady-state behavior with the transient motion. A determination of the complete rotor trajectory is more costly than the linear stability analysis but by the use of the approximate procedure the computer costs are reasonable.

The transient path is obtained by integrating equations (22) and (23) forward in time. This is accomplished by solving equations (22) and (23) for the components of acceleration $\ddot{X}$ and $\ddot{Y}$.

The integration may be accomplished by the use of the Adams-Bashforth-Moulton predictor–corrector procedure with a 6th order Runge-Kutta starter as used by Kirk [5] or the modified Euler method of Castelli [9]. If rotor acceleration is included, then it is necessary to use a predictor–corrector procedure in order to incorporate a variable time step.

The Euler method with constant time step as used in this analysis is given as follows.

$$\dot{X}(T + \Delta T) = \dot{X}(T) + \ddot{X}(T)\cdot\Delta T \tag{34}$$

$$\dot{Y}(T + \Delta T) = \dot{Y}(T) + \ddot{Y}(T)\cdot\Delta T \tag{35}$$

The components of displacement are found by integrating the velocity expressions with the modified Euler method.

$$X(T + \Delta T) = X(T) + \dot{X}(T + \Delta T)\cdot\Delta T \tag{36}$$

$$Y(T + \Delta T) = Y(T) + \dot{Y}(T + \Delta T)\cdot\Delta T \tag{37}$$

The predicted velocity and displacement components are then substituted into equation (10) for the determination of the bearing pressure profile, and by means of equation (14) the hydrodynamic force components are obtained. The use of the approximate method in determining the hydrodynamic bearing forces provides an excellent means of calculating the rotor transient motion since it has an execution rate about 100 times faster than the finite bearing method. The transient orbit analysis was used to verify the observed stability thresholds for various experimental data points. For example in the experimental case with the preload of 0.70 and a bearing clearance of 6.6 mil, the measured stability was 800 rpm which corresponds to a critical mass of 6.63. The finite-width multi-lobe bearing stability program predicts an upper stability threshold of 834 rpm for small perturbations with the transition region beginning at approximately 500 rpm. Using the approximate stability method, the critical mass is calculated to be 5.70 which corresponds to a threshold speed of 687 rpm.

To investigate the behavior of the rotor system below and above the stability threshold, the time transient orbit program was used. For example Fig. 9 represents the transient motion of the vertical rotor in a three-lobe bearing below the threshold for the case of $C = 6.6$ mil with an offset factor of approximately 0.7. The dotted line in the figure represents the minimum bearing clearance circle. The test case was started with an initial dimensionless displacement of $X = 0.1$ and a rotor speed of 500 rpm. The transient path of the rotor moves from the initial displacement to the bearing origin indicating a stable configuration. This corresponds to the predicted performance since the system is operating below the threshold of stability. Fig. 10 represents the motion of the rotor system operating at a speed of 1000 rpm which is above the predicted stability threshold. The rotor is given an initial X displacement and the orbit is increasing with time indicating an unstable system. To further indicate self-excited instability, timing marks are placed on the orbit after every shaft cycle. The positioning of the various timing marks indicates whether synchronous or nonsynchronous

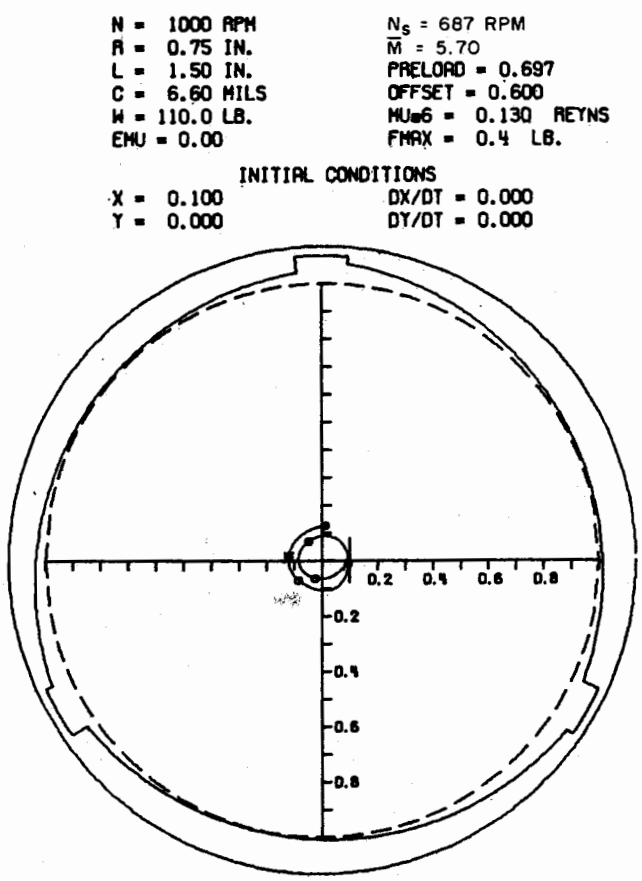

Fig. 10 Initial transient orbit of a balanced vertical rotor above the stability threshold, $N = 1000$, $N_s = 687$ rpm

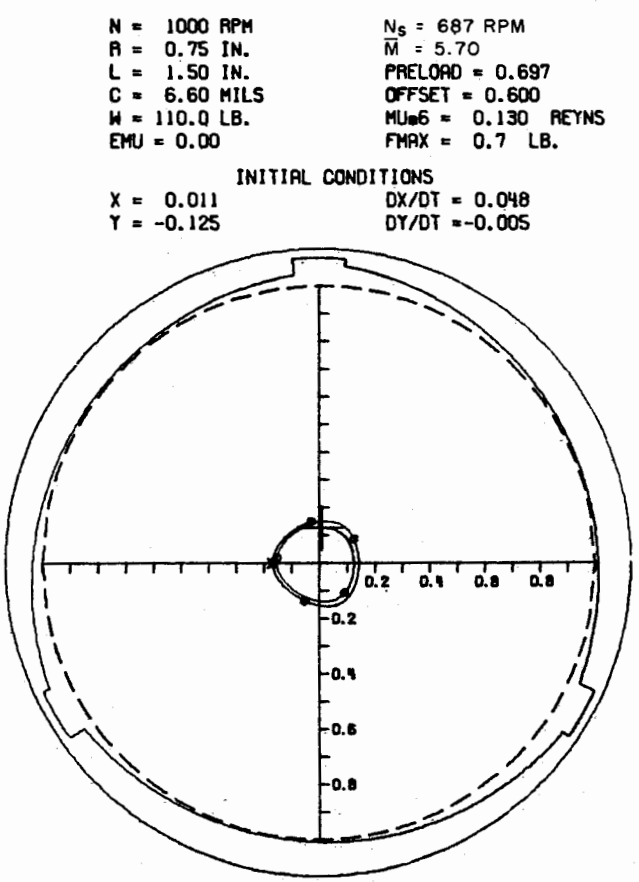

Fig. 11 Limit cycle motion of a balanced vertical rotor above the stability threshold, $N = 1000$, $N_s = 687$ rpm

precession is occurring. Fig. 11 is a continuation of Fig. 10 for an additional five cycles of shaft motion and it can be seen that a limit cycle will occur. The frequency of precession is about 0.4 of the speed of rotation. Even though the rotor is operating above the stability threshold, the nonlinear transient analysis indicates that it can operate with a finite limit cycle. Various computer runs conducted indicated that the multi-lobe bearing can quite often operate well above the predicted threshold of stability with a small finite limit cycle. In general the higher the rotor is operated above the stability threshold, the larger will be the rotor limit cycle with correspondingly higher forces transmitted to the bearing.

The transient analysis developed in this work has the ability to evaluate rotor unbalance or any arbitrary loading such as impulse or shock forces. For example, Fig. 12 represents a vertical unbalanced rotor in which the unbalance eccentricity is 80 percent of the bearing sector clearance. Since the shaft is operating well below the stability threshold the rotor forms a synchronous whirl orbit which is indicated by all the timing marks occurring at one position. Note that the orbit is not circular but has a three-lobed pattern corresponding to the bearing configuration. Such an orbital pattern cannot be predicted by linear bearing theory. The rotating unbalance load is 30.2 lb and the maximum force developed is 37.2 lb which corresponds to a dynamic transmissibility TRD = 1.23. The position of the maximum force is denoted by the asterisk in the figure.

Fig. 13 is similar to the previous cases except the unbalance has been removed and the rotor speed has been increased to well above the stability threshold. The resulting orbit moves from the initial displacement of $X = 0.1$ to the indicated three-sided limit cycle. By the observation of the timing marks it can be seen that the average whirl frequency is somewhat less than one-half. The limit cycle in this case is obtained after only six cycles of shaft motion. If a small unbalance is now added to the rotor as shown in Fig. 14, then a large initial transient motion will occur which decreases with time until a small radius orbit with synchronous precession is attained. The small unbalance force causes a maximum force of 131 lb to be transmitted during the first cycle of shaft motion.

If the shaft unbalance is increased from EMU = 0.2 to 0.8, then the shaft nonsynchronous motion is rapidly suppressed and only synchronous precession remains in the system as shown in Fig. 15. The maximum force transmitted to the bearing is now 738.4 lb, corresponding to a TRD = 2.87 for a speed of 7000 rpm in comparison to the 37.2 lb for a speed of 2400 rpm. Thus, because of the bearing nonlinearity, the increase of rotor speed by a factor of about three has caused the bearing forces to increase by almost a factor of 20. Therefore, stabilization of the shaft system by the addition of large unbalance is not recommended because of the high transmitted forces.

Optimization of a Vertical Three-Lobed Bearing

Fig. 8 indicated that the critical mass increases as preload is increased but does not indicate an optimum value of preload for the particular bearing configuration. The preload factor can be optimized by cross-plotting the analytical data of Fig. 8. Fig. 16 is a cross-plot obtained by plotting threshold speed against bearing clearance for various values of preload. This is accomplished by selecting a value of clearance C and solving for the threshold speed corresponding to given values of $\bar{M}$ and δ. This produces lines of constant δ on a log–log plot. The minimum film thickness h_m is equal to $C(1 - \delta)$ and a family of

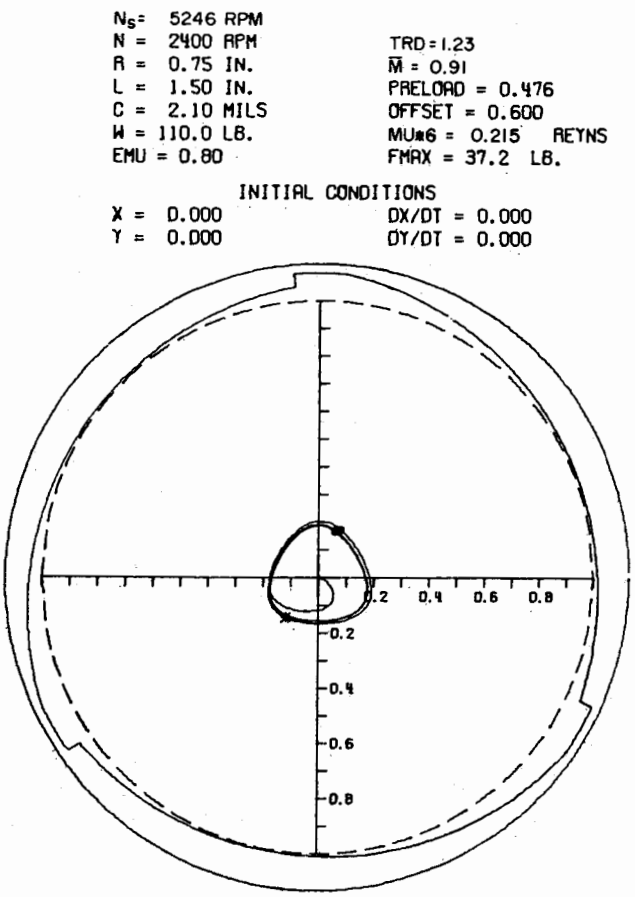

Fig. 12 Transient motion of an unbalanced vertical rotor below the stability threshold depicting synchronous precession, EMU = 0.8, N = 2400, N_s = 5245 rpm

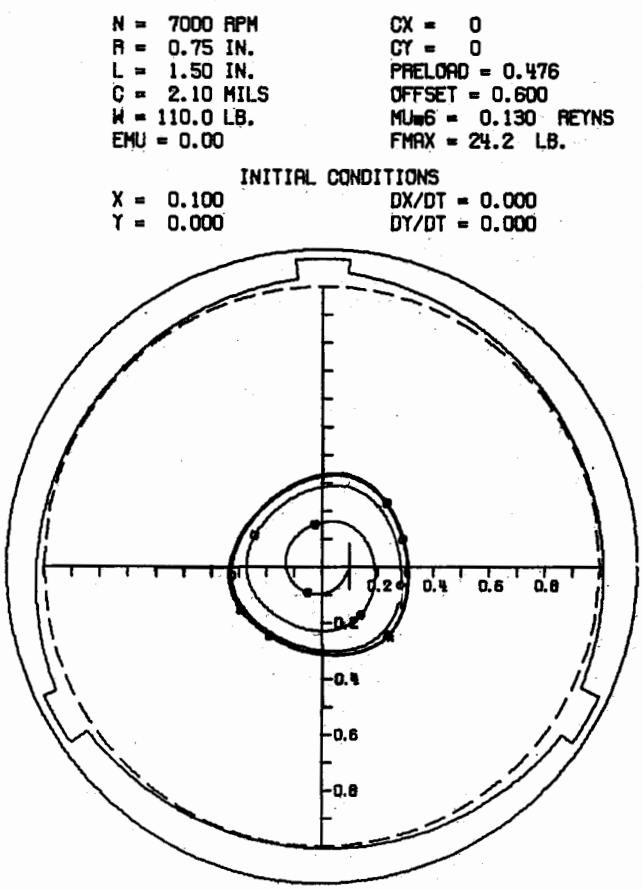

Fig. 13 Initial transient orbit of a balanced vertical rotor above the stability threshold depicting fractional-frequency whirl, N = 7000, N_s = 5246

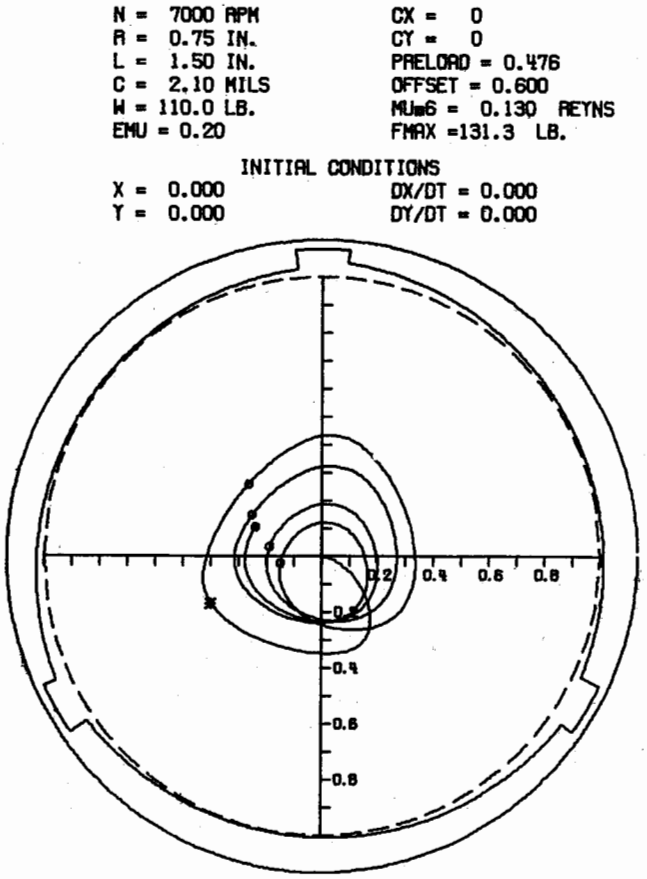

Fig. 14 Initial transient motion of a vertical rotor with moderate unbalance operating above the stability threshold, EMU = 0.2, N = 7000, N_s = 5246, E_m = 0.2

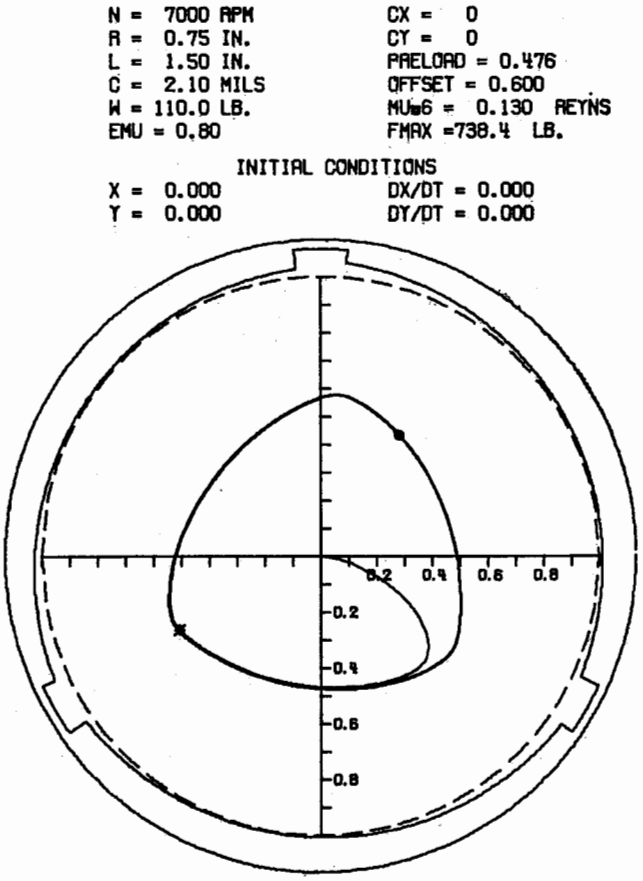

Fig. 15 Transient orbit of a vertical rotor with large unbalance causing synchronous precession above the stability threshold, EMU = 0.8, N = 7000, N_s = 5246 stability

minimum film thickness curves can be produced. It is now possible to determine the optimum preload corresponding to the highest threshold speed for a given value $h_{\min}$. Fig. 16 shows that the optimum value of preload for an offset factor of 0.6 is about $\delta_{opt} = 0.66$. Rather than construct a figure similar to Fig. 16 for each value of offset factor, it is possible to define a modified stability mass and plot it against preload factor to determine the optimum amount of preload. The selection of M_{Hm} is arrived at by noting that $\bar{M}$ is a function of C^3 and $h_m = (1 - \delta)$ thus M_{Hm} is equal to $\bar{M}$ with C replaced by h_m. Fig. 17 represents a plot of the modified mass parameter versus preload for various values of offset factor α ranging from 0.6 to 1.2. For the case of the converging–diverging film geometry $\alpha = 0.6$, it is seen that the optimum preload is approximately 0.66. As the offset factor increases from 0.6 to 1.0, the stability parameter increases as verified by experimental data and the corresponding optimum preload decreases from 0.66 to 0.47. Note that if the film convergence is increased beyond $\alpha = 1.0$, the effective stability is decreased. Therefore it appears that the optimum bearing configuration for a vertical unloaded rotor would have a preload between 0.47 and 0.59 corresponding to offset factors ranging from 1.0 to 0.8.

Thus a good approximation of the stability threshold of a vertical three-lobe bearing of $L/D = 1.0$ with an offset factor of $\alpha = 1.0$ with optimum preload of 0.5 is given by

$$N_{\text{rpm}} = \frac{300\,\mu L}{M}\left(\frac{R}{C}\right)^3 \tag{38}$$

Conclusions

1 It is possible to accurately predict the performance characteristics of a multi-lobe bearing by means of an infinite bearing solution corrected for end leakage.

2 The accuracy of the approximate finite bearing solution decreases as the aspect ratio approaches zero and also decreases with high eccentricities.

3 From a practical standpoint the use of the approximate finite bearing solution in a transient analysis of a rotor-bearing system yields acceptable results with a reduction in computer run time by a factor of 100 over the numerical finite-difference method.

4 There appears to exist a transition region of stability which is dependent upon the magnitude of the velocity perturbation. The consequence of this phenomena in a physical system is that a hysteresis region may exist in the stability threshold.

5 A balanced vertical rotor in an axial groove bearing is unstable at all speeds.

6 For a given film geometry or offset factor α, the stability increases with preload.

7 The optimum design based on minimum film thickness of a three-lobe bearing configuration should have a film geometry with the offset factor ranging from 0.8 to 1.0 and a corresponding preload factor varying from 0.59 to 0.47.

8 The rotor-bearing system may operate considerably above the predicted stability threshold speed by forming a limit cycle.

9 As the speed is increased above the stability threshold, the size of the journal limit cycle increases as well as the forces transmitted to the bearing.

10 Introduction of large rotor unbalance can suppress the nonsynchronous whirl motion when operating above the stability threshold. It is not recommended to stabilize a rotor by this method because of the large forces transmitted.

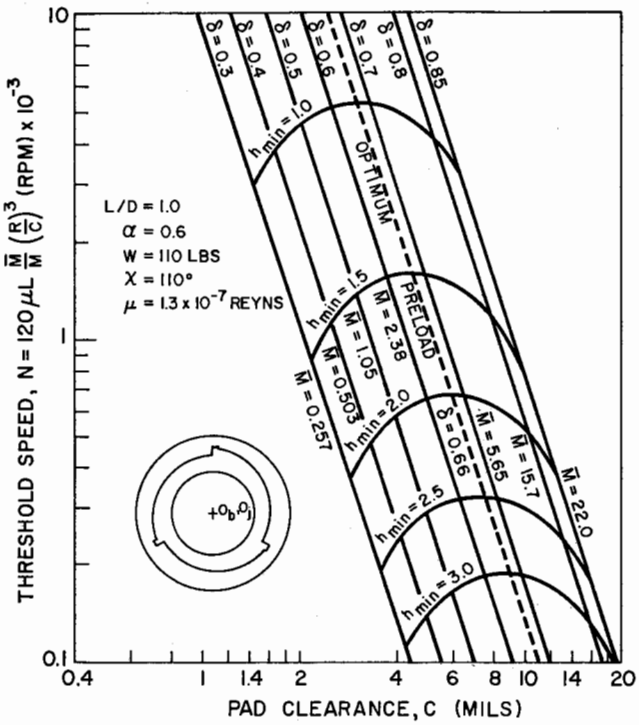

Fig. 16 Threshold speed versus bearing clearance for a vertical rotor in a three-lobe bearing for various values of preload and minimum film thicknesses

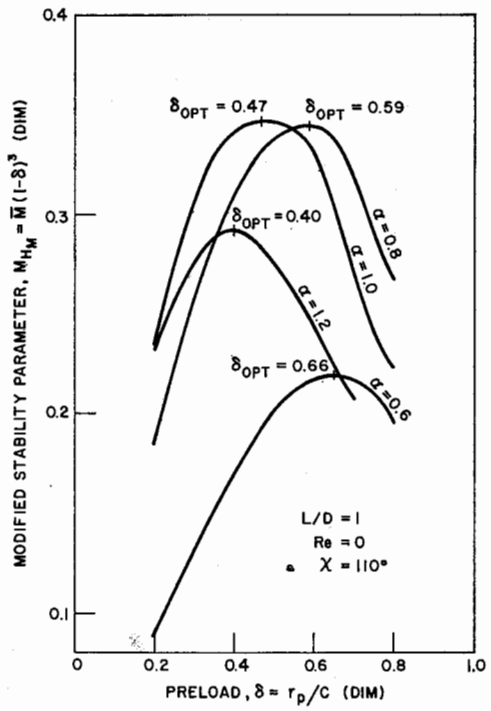

Fig. 17 Modified stability mass parameter versus preload for a three-lobe bearing L/D = 1.0, Re = 0, χ = 110 deg

11 The orbit shape is influenced by the number of lobes in the bearing.

12 The bearing theory using linearized stiffness and damping coefficients cannot predict the shape of the orbits obtained with the multi-lobe bearing nor can it accurately predict the bearing forces transmitted.

Acknowledgments

The research described herein was conducted at NASA Lewis Research Center and at the University of Virginia, under NASA Research Grant NGR 47-005-050 with Mr. William J. Anderson, chief of Bearings Branch, Fluid System Components Div., NASA Lewis Research Center, as technical manager. The authors wish to express their thanks to Mr. Anderson for his assistance and constant encouragement in the development of this work.

The authors also wish to express their appreciation to R. Gordon Kirk of the University of Virginia for his assistance in programming the automatic plotter routines and numerical time transient integration procedures used in this investigation.

References

1 Pinkus, O., "Analysis and Characteristics of the Three-Lobe Bearing," *Journal of Basic Engineering*, TRANS. ASME, Series D, Vol. 81, No. 1, Mar. 1959, pp. 49–55.

2 Pinkus, O., "Power Losses in Elliptical and 3-Lobe Bearings," TRANS. ASME, Vol. 78, 1956, pp. 899–904.

3 Pinkus, O., "Experimental Investigation of Resonant Whip," TRANS. ASME, Vol. 78, 1956, pp. 975–983.

4 "Rotor-Bearing Dynamics Design Technology, Part III: Design Handbook for Fluid Film Type Bearings," Technical Report AFAPL-TR-65-45, May 1965, Wright-Patterson Air Force Base, Ohio.

5 Kirk, R. G., and Gunter, E. J., "Transient Journal Bearing Analysis," NASA CR-1549, Clearinghouse for Federal Scientific and Technical Information, Springfield, Va., June 1970.

6 Lund, J., "Rotor-Bearing Dynamics Design Technology, Part VII: The Three-Lobe Bearing and Floating Ring Bearing," Technical Report AFAPL-TR-65-45, Feb. 1968, Wright-Patterson Air Force Base, Ohio.

7 Falkenhagen, G., and Gunter, E. J., "Non-Linear Transient Analysis of a Rigid Rotor Supported by Non-Circular Bearings," Research Laboratories for Engineering Sciences, University of Virginia, Charlottesville, Va., ME-4040-102-70U, June 1970.

8 Castelli, V., and Elrod, H. G., "Solution of the Stability Problem for 360 Deg Self-Acting, Gas-Lubricated Bearings," *Journal of Basic Engineering*, TRANS. ASME, Series D, Vol. 87, No. 1, Mar. 1965, pp. 199–212.

9 Castelli, V., and McCabe, J. T., "Transient Dynamics of a Tilting Pad Gas Bearing System," *Journal of Lubrication Technology*, TRANS. ASME, Series F, Vol. 89, No. 3, Oct. 1967, pp. 499–509.

10 Raimondi, A., and Boyd, J., "A Solution for the Finite Journal Bearing and its Application to Analysis and Design—II and III," *Trans. ASLE*, Vol. 1, No. 1, 1958.

11 Pinkus, O., "Solution of Reynolds Equation for Arbitrarily Loaded Journal Bearings," *Journal of Basic Engineering*, TRANS. ASME, Series D, Vol. 83, No. 2, June 1961, pp. 145–152.

12 Castelli, V., and Shapiro, W., "Improved Method for Numerical Solutions of the General Incompressible Fluid Film Lubrication Problem," *Journal of Lubrication Technology*, TRANS. ASME, Series F, Vol. 89, No. 2, Apr. 1967, pp. 211–218.

13 Castelli, V., and Pirvics, J., "Review of Numerical Methods in Gas Bearing Film Analysis," *Journal of Lubrication Technology*, TRANS. ASME, Series F, Vol. 90, No. 4, Oct. 1968, pp. 777–792.

14 Pitts, G., "An Analytical Study of the Tilting Pad Gas Lubricated Journal Bearing," *Proc. Inst. Mech. Engrs.*, 1966–67, Vol. 181, Pt. 1, No. 13, pp. 293–300.

15 Pinkus, O., and Sternlicht, B., *Theory of Hydrodynamic Lubrication*, McGraw-Hill, New York, N.Y., 1961, pp. 88–89.

16 Gunter, E. J., Hinkle, J. G., and Fuller, D. D., "Design Guide for Gas-Lubricated Tilting-Pad Journal and Thrust Bearings With Special Reference to High-Speed Rotors," NYO-2512-1, The Franklin Institute, I-A2392-3-1, Nov. 1964.

17 Gunter, E. J., "Dynamic Stability of Rotor-Bearing Systems," NASA SP-113, 1966.

18 Schuller, F. T., and Anderson, W. J., "Experiments on the Stability of Water-Lubricated Three-Sector Hydrodynamic Journal Bearings at Zero Load," NASA TN D-5752, Lewis Research Center, Cleveland, Ohio, Apr. 1970.

APPENDIX A

Derivation of Multi-Lobed Bearing Film Thickness in Fixed Coordinates

For the bearing and shaft of Fig. 2 let P be a point on the shaft and Q be a corresponding radial point on the bearing. The local

film thickness will be defined as the radial component of the position vector between points P and Q.

The position vector from the bearing origin 0 to a point Q on the first bearing sector is given by

$$\mathbf{P}_Q = \mathbf{P}_{0_1} + \mathbf{P}_{Q_1 0_1} = r_p \mathbf{n}_{r_c} + (R + C)\mathbf{n}_r \tag{39}$$

The unit vectors $\mathbf{n}_r$ and $\mathbf{n}_{r_c}$ may be expressed in terms of the fixed cartesion unit vectors $\mathbf{n}_X$ and $\mathbf{n}_Y$, thus

$$\mathbf{P}_Q = [(R + C)\cos\theta - r_p \cos\theta_c]\mathbf{n}_X + [(R + C)\sin\theta - r_p \sin\theta_c]\mathbf{n}_Y \tag{40}$$

The position vector to the point P on the shaft is given in terms of the journal eccentricity and shaft radius vectors as follows:

$$\mathbf{P}_P = \mathbf{e} + R\mathbf{n}_r \tag{41}$$

The eccentricity vector $\mathbf{e}$ may be expressed in terms of the X, Y displacements of the journal center. The position vector to point P is thus expressed as follows

$$\mathbf{P}_P = (X + R\cos\theta)\mathbf{n}_X + (Y + R\sin\theta)\mathbf{n}_Y \tag{42}$$

The local film thickness for the first sector is thus given by

$$h(\theta) = (\mathbf{P}_Q - \mathbf{P}_P)\cdot\mathbf{n}_r = [(C\cos\theta - X - r_p\cos\theta_c)\mathbf{n}_X + (C\sin\theta - Y - r_p\sin\theta_c)\mathbf{n}_Y]\cdot[\cos\theta\mathbf{n}_X + \sin\theta\mathbf{n}_Y] = C - X\cos\theta - Y\sin\theta - r_p\cos(\theta_c - \theta) \tag{43}$$

APPENDIX B

Development of the End-Leakage Correction Parameter K

The end-leakage correction parameter K for the partial arc bearing of Fig. 1 is developed in the following manner. The steady-state incompressible Reynolds equation, in polar coordinates, is

$$\frac{\partial}{\partial\theta'}\left(H^3\frac{\partial p}{\partial\theta'}\right) + \left(\frac{R}{L}\right)^2\frac{\partial}{\partial\eta}\left(H^3\frac{\partial p}{\partial\eta}\right) = \lambda\frac{\partial H}{\partial\theta'} \tag{44}$$

where

$$H = 1 + \epsilon\cos\theta'$$

In terms of $\psi = pH$, equation (44) becomes

$$\frac{\partial}{\partial\theta'}\left(H^3\frac{\partial\frac{\psi}{H}}{\partial\theta'}\right) + \left(\frac{R}{L}\right)^2\frac{\partial}{\partial\eta}\left(H^3\frac{\partial\frac{\psi}{H}}{\partial\eta}\right) = \lambda\frac{\partial H}{\partial\theta'} \tag{45}$$

Assuming no misalignment, then $\frac{\partial H}{\partial\eta} = 0$ and dividing by H^2 equation (45) becomes:

$$\frac{\partial^2\psi}{\partial\theta'^2} + \left(\frac{R}{L}\right)^2\frac{\partial^2\psi}{\partial\eta^2} + \frac{1}{H}\frac{\partial H}{\partial\theta'}\frac{\partial\psi}{\partial\theta'} - \frac{\psi}{H^2}\left(\frac{\partial H}{\partial\theta'}\right)^2 - \frac{\psi}{H}\frac{\partial^2 H}{\partial\theta'^2} = \lambda\frac{\partial H}{\partial\theta'} \tag{46}$$

but

$$H = 1 + \epsilon\cos\theta', \quad \frac{\partial H}{\partial\theta'} = -\epsilon\sin\theta', \quad \frac{\partial^2 H}{\partial\theta'^2} = -\epsilon\cos\theta'$$

hence

$$\frac{\partial^2\psi}{\partial\theta'^2} + \left(\frac{R}{L}\right)^2\frac{\partial^2\psi}{\partial\eta^2} - \frac{\epsilon\sin\theta'}{1 + \epsilon\cos\theta'}\frac{\partial\psi}{\partial\theta'} - \left[\frac{\epsilon\sin\theta'\psi}{1 + \epsilon\cos\theta'}\right]^2\psi + \frac{\epsilon\cos\theta'}{1 + \epsilon\cos\theta'}\psi = -\lambda\epsilon\sin\theta' \tag{47}$$

Equation (47) is a differential equation with variable coefficients. These variable coefficients are replaced by average values tained by integration over the sector arc length as follows:

$$A = \frac{1}{\chi}\int_\xi^\beta \frac{\epsilon\sin\theta'}{1 + \epsilon\cos\theta'}\,d\theta' \tag{48}$$

$$B = \frac{1}{\chi}\int_\xi^\beta \left\{\left[\frac{\epsilon\sin\theta'}{1 + \epsilon\cos\theta'}\right]^2 - \frac{\epsilon\cos\theta'}{1 + \epsilon\cos\theta'}\right\}d\theta' \tag{49}$$

$$D = \frac{1}{\chi}\int_\xi^\beta \epsilon\sin\theta' d\theta' \tag{50}$$

Equation (47) can thus be approximated by the following differential equation with constant coefficients

$$\frac{\partial^2\psi}{\partial\theta'^2} + \left(\frac{R}{L}\right)^2\frac{\partial^2\psi}{\partial\eta^2} - A\frac{\partial\psi}{\partial\theta'} - B\psi = -\lambda D \tag{51}$$

For the infinite bearing, equation (51) becomes

$$\frac{\partial^2\psi_\infty}{\partial\theta'^2} - A\frac{\partial\psi_\infty}{\partial\theta'} - B\psi_\infty = -\lambda D \tag{52}$$

Assume a solution for the finite bearing of the following form:

$$\psi = \psi_\infty + M(\theta')N(\eta) \tag{53}$$

where M is a function of θ' only and N is a function of η only. Substituting equation (53) into equation (48) and substracting equation (52)

$$\frac{\partial^2(MN)}{\partial\theta'^2} + \left(\frac{R}{L}\right)^2\frac{\partial^2(MN)}{\partial\eta^2} - A\frac{\partial(MN)}{\partial\theta'} - BMN = 0 \tag{54}$$

differentiating and dividing by MN

$$-\frac{\left(\frac{R}{L}\right)^2\frac{d^2N}{d\eta^2}}{N} = \frac{\frac{d^2M}{d\theta'^2}}{M} - \frac{A\frac{dM}{d\theta'}}{M} - B = K^2 \tag{55}$$

where K is the constant of separation.

Solving equation (55) for

$$\frac{d^2N}{d\eta^2} - K^2N\left(\frac{L}{R}\right)^2 = 0 \tag{56}$$

The general solution to equation (56) for N is

$$N = B_3\sinh\left(\frac{KL}{R}\right)\eta + C_3\cosh\left(\frac{KL}{R}\right)\eta \tag{57}$$

The boundary conditions require that the maximum pressure occur at $\eta = 0$ which can be expressed mathematically as $\frac{dN}{d\eta} = 0$ at $\eta = 0$. Applying this condition to equation (57), the constant B_3 is found to be zero and the solution to equation (56) is

$$N = C_3\cosh\left(\frac{KL}{R}\right)\eta \tag{58}$$

Writing equation (55) in standard form for M

$$\frac{d^2M}{d\theta'^2} - A\frac{dM}{d\theta'} + M(K^2 - B) = 0 \tag{59}$$

The auxiliary equation for equation (59) is given by

$$D^2 - AD + (K^2 - B) = 0 \tag{60}$$

from which

$$D = \frac{A \pm \sqrt{A^2 - 4(K^2 - B)}}{2} \tag{61}$$

assuming that $4(K^2 - B) > A^2$, then the auxiliary equation has complex roots and the general solution to equation (59) is

$$M = e^{\frac{A}{2}\theta'} [B_4 \cos K_1\theta' + C_4 \sin K_1\theta'] \tag{62}$$

where

$$K_1 = \sqrt{K^2 - B - \left(\frac{A}{2}\right)^2} \tag{63}$$

The appropriate boundary conditions for the circumferential direction are

$$M = 0 \qquad \theta' = \xi$$

$$M = 0 \qquad \theta' = \xi + \chi = \beta$$

Substitution of these boundary conditions into equation (62) results in the following system of equations:

$$\begin{bmatrix} \cos K_1\xi & \sin K_1\xi \\ \cos K_1\beta & \sin K_1\beta \end{bmatrix} \begin{bmatrix} B_4 \\ C_4 \end{bmatrix} = 0$$

The above system of equations has a nontrivial solution when the determinant of the coefficient matrix vanishes. Hence

$$\cos K_1\xi \sin K_1\beta - \cos K_1\beta \sin K_1\xi \tag{64}$$

which is equivalent to requiring

$$\sin K_1(\beta - \xi) = 0 \tag{65}$$

Equation (65) has multiple solutions of the form

$$K_1(\beta - \xi) = n\pi \qquad n = 1, 2, \ldots \tag{66}$$

Solving equation (66) for K_1

$$K_1 = \frac{n\pi}{\beta - \xi} = \frac{n\pi}{\chi} \qquad n = 1, 2, \ldots \tag{67}$$

Substituting equation (67) into equation (62) and transforming the origin so that only the sine term remains, the solution becomes

$$M = e^{\frac{A}{2}(\theta' - \xi)} \sum_{n=1}^{\infty} C_4 \sin K_1(\theta' - \xi) \tag{68}$$

Taking the first harmonic of equation (68) and equation (58) and substituting these relations into equation (53)

$$\psi = \psi_\infty + C_5 e^{\frac{A}{2}} (\theta' - \xi) \sin \frac{\pi}{\chi} (\theta' - \xi) \cosh \frac{KL}{R} \eta \tag{69}$$

where K is determined from equations (63) and (67) to be

$$K = \sqrt{\left(\frac{\pi}{\chi}\right)^2 + \left(\frac{A}{2}\right)^2 + B} \tag{70}$$

Equation (70) is the expression for the end-leakage correction parameter.

Equation (69) can be written as

$$\psi = \psi_\infty + f(\theta') \cosh \frac{KL}{R} \eta \tag{71}$$

The boundary conditions at either end of a finite lobe are ambient from which

$$\psi = 0 \quad \text{at} \quad \eta = \pm\frac{1}{2}$$

Substituting this condition into equation (71)

$$f(\theta') = -\frac{\psi_\infty}{\cosh \frac{KL}{D}} \tag{72}$$

Substituting equation (72) into equation (71) and dividing by H

$$p = p_\infty \left[1 - \frac{\cosh \frac{KL}{R} \eta}{\cosh \frac{KL}{D}} \right] \tag{73}$$

Equation (73) indicates the manner in which the infinite bearing pressure distribution is corrected for end leakage.

DISCUSSION

W. Shapiro[2]

The authors attempt to demonstrate by Fig. 8 that theoretical stability is a function of the size of the velocity disturbances. The only way this is manifest in the analysis is in establishing damping coefficients for equation (28). In fact, the stability analysis (solution of equation (28)) is a small perturbation linearized treatment and spring and damping values must be constant for the analysis to be valid, irrespective of how Reynold's equation is solved to obtain these coefficients. Shown in Fig. 18 is a hypothetical curve of force response, F versus velocity, V, of a bearing. If the bearing was operating at point 1, the damping coefficient is the slope of the tangent to the curve at point 1. If too large a velocity perturbation is made such as from 1 to 2, the slope of the line through these points would be the resultant damping coefficient and could be grossly in error. As a matter of fact, one way to determine a proper magnitude for the perturbation is to insure that $\Delta F/\Delta V$ remains a constant. If not, a smaller perturbation is necessary. Thus, the large velocity perturbations stability threshold curve on Fig. 8 is in error and results from improper determination of the damping coefficients used in equation (28).

The use of side leakage factors is questioned especially when approximate analysis is used for establishing damping characteristics. The computations of Appendix B do not include squeeze film leakage.

---

[2] Manager, Friction & Lubrication Laboratory, The Franklin Institute Research Laboratories, Philadelphia, Pa. Mem. ASME.

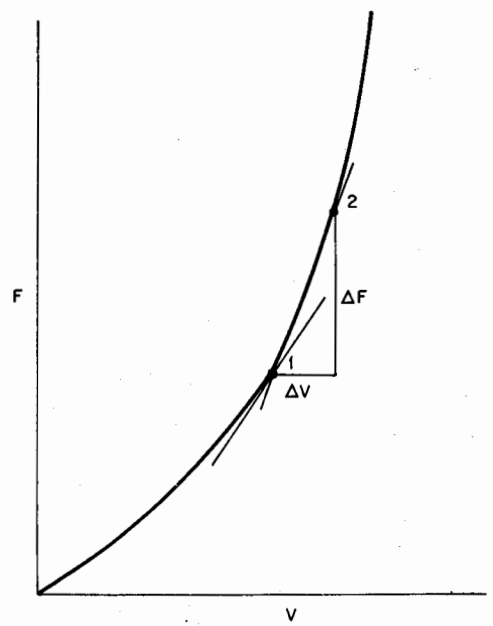

Fig. 18

The discusser does agree with the motivation behind the approximate bearing treatment, namely to reduce computer time in orbit analyses. This can be accomplished, however, without resorting to approximations. For an incompressible bearing, field maps can be generated that relate load capacity and normalized squeeze film capacity as a function of the journal position. Interpolation of these field maps at each time step then provides very accurate film characteristics. Savings in computational time over the numerical process that solves Reynold's equation at each time step is on the order of 100/1.

In conclusion, the discusser would like to compliment the authors on a very comprehensive study and vivid demonstration of the power and advantages of computerized analysis for solving difficult dynamic problems.

Author's Closure

The authors wish to express their appreciation to Mr. Shapiro for his interest and comments on the paper. The stability of a hydrodynamic bearing may be calculated either by linearizing the Reynolds equation as described in reference [6] or by calculation of the incremental force variations of the complete Reynolds equation for small displacement and velocity components. The point that the authors wish to emphasize is that changes of velocity perturbation quantity alter the stability characteristics. This results in a band of stability based on the magnitude of the velocity perturbation which cannot be obtained from the linearized Reynolds equation. Such a behavior has been reported by Badgely and Booker [19][3] in their paper on the effect of initial transients on the stability characteristics of the plain journal bearing. For example, Badgely and Booker found out that for values of the stability parameter ω/ω_g greater than 2.5 the rotor would be stable at an eccentricity of 0.7 for small velocity disturbances but would not stabilize until an eccentricity greater than 0.8 was obtained for large initial velocity disturbances.

Such a characteristic behavior has been observed in the laboratory on bearing performance. The authors feel that it is important to calculate the stability threshold based on small and large velocity disturbances. For example, the rotor may be operating below the stability threshold based on small velocity perturbations but above the stability threshold for large velocity perturbations. The rotor will appear to be stable for a small displacement but if given a large transient excitation a large whirl orbit will result as has been shown by various computer runs. The rotor system under these conditions would be very shock sensitive.

Mr. Shapiro correctly notes that the side leakage factor is based upon steady state operation and therefore does not include the squeeze film leakage effect. Comparison of the approximate to the two dimensional numerical solution for various cases seemed to indicate good agreement.

Mr. Shapiro states that orbit analysis may be efficiently performed by means of field maps that are generated from the numerical solution that relate load capacity and normalized squeeze film capacity as a function of the journal position. A similar concept has been utilized previously by Booker in his mobility studies of the plain journal bearing in which he generates field maps of bearing load capacity and the squeeze film damping terms [20]. In general the forces generated in a hydrodynamic bearing are a function of four variables, the journal displacements x and y, and the velocity components $\dot{x}$ and $\dot{y}$. The situation is further complicated if cavitation is taken into consideration. For example extensive field maps were presented in reference [16] on the steady state characteristics of partial and tilting pad bearings. At the time it was not certain how this data could be used for dynamic studies. It is difficult for the authors to comprehend how field maps incorporating four distinct variables and cavitation can be accurately interpolated for use in a dynamics analysis. If Mr. Shapiro has developed a procedure in which this can be done accurately and rapidly it would be most advantageous in bearing dynamics studies as the Reynolds equation would not have to be calculated at each time step. We will be looking forward to seeing future presentations of this material by Mr. Shapiro.

[3] Numbers in brackets designate Additional References at end of closure.

Additional References

19 Badgley, R. H. and Booker, J. F., "Turborotor Instability—Effect of Initial Transients on Plane Motion," *Journal of Lubrication Technology*, Trans. ASME, Series F, Vol. 91, No. 4, Oct. 1969, pp. 625–633.

20 Booker, J. F., "Dynamically Loaded Journal Bearings, Mobility Method of Solution," *Journal of Basic Engineering*, TRANS. ASME, Series D, Vol. 87, No. 3, Sept. 1965, pp. 537–546.